# Wetting on heterogeneous surfaces: Experiments in an imperfect Hele-Shaw cell

A. Paterson, M. Fermigier, P. Jenffer, and L. Limat
*Laboratoire de Physique et Mécanique des Milieux Hétérogènes, Ecole Supérieure de Physique et de Chimie Industrielles de la Ville de Paris,*
*10 rue Vauquelin, 75231 Paris Cedex 05, France*
(Received 24 May 1994; revised manuscript received 14 October 1994)

We use a model system, a thin Hele-Shaw cell, to study the influence of surface wettability defects on the behavior of a liquid front advancing on a substrate. Defects are made by deposition of ink droplets on a glass surface. We record the deformation of the interface of a silicone oil displacing air in the cell, at very small capillary numbers. There is a trapping transition determined by the defect strength. The contact line cannot move over defects that are too large and an air bubble remains trapped on the defect. Smaller defects do hold the contact line for a while, but they are eventually wetted by the advancing liquid. From the shape of the contact line anchored on a single defect we determine the energy associated with the line deformation. From the experimental energy-displacement curves we find that the force exerted by the defect on the contact line increases linearly with the deformation. We also determine the amplitude of fluctuation of the interface when it moves over multiple defects. When the average defect strength is larger than the critical value, air bubbles with a size up to the capillary length are trapped by the defects.

PACS number(s): 68.10.−m, 47.55.Kf, 05.40.+j

## I. INTRODUCTION

Wetting phenomena and wetting dynamics control many industrial processes. In particular, coating flows and enhanced oil recovery are somehow controlled by the motion of the contact line, i.e., the intersection of the fluid-fluid interface and the solid surface. Many recent studies have been devoted to the theoretical and experimental investigations of wetting dynamics [1]. The dynamics of wetting of clean and smooth surfaces is now well understood. However, in most situations of practical interest, solid surfaces are rough and chemically heterogeneous. Even in the microelectronics industry, coating integrated circuits with a protective polymeric layer might be influenced by surface defects [2]. In space, where gravity is completely negligible, defects on container walls can play an important role on the fluid motion [3]. The flotation of fine solid particles is also influenced by the pinning of the contact line on surface heterogeneities [4]. Wettability defects can also drastically alter the quality of adhesive bonding [5].

Roughness and heterogeneity account for the existence of contact angle hysteresis: the static angle between the solid surface and the fluid interface is found to be different when the contact line advances and when the contact line recedes. For example, Lazare *et al.* [6] demonstrated the influence of photoinduced roughening on the contact angle of water deposited on a polyethyleneterephtalate substrate.

Surface defects also influence the dynamics of the contact line: the line is held on less wettable spots and released later. Contact line trapping produces a fluctuating force on the contact line. Force measurements on a fiber drawn out of a bath of liquid [7] showed that the square of the force fluctuation varies linearly with the contact angle hysteresis $\cos\theta_a - \cos\theta_r$.

Recently we and several other groups attacked the problem of wetting on heterogeneous surfaces by investigating the interaction of a moving contact line with artificial defects [8–11]. The goal of the present study is to assess the influence of surface defects on, first, the amplitude and statistics of the contact line fluctuations, second, the amount of solid surface covered by the advancing liquid, and, finally, the mean wetting speed. The crucial step of this work is to prepare a well characterized system with controlled surface defects. We use an "imperfect Hele-Shaw cell," introduced by de Gennes [12] as a model system for a porous medium (Fig. 1). A liquid-gas interface moves in a very thin rectangular cell of thickness $h$. One of the cell walls has surface defects of average diameter $d$.

The wettability of the solid is gauged by the spreading coefficient $S = \gamma_{sg} - \gamma_{sl} - \gamma$, where $\gamma_{ij}$ is the surface ten-

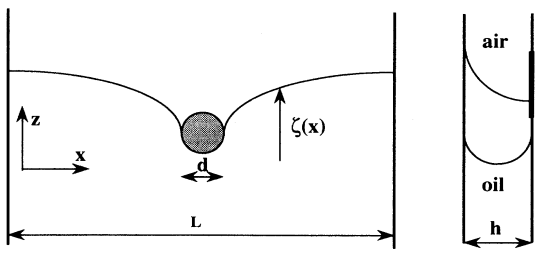


FIG. 1. Geometry of the imperfect Hele-Shaw cell. Front view on the left, showing the distorted contact line pinned on a single defect. Side view on the right, showing two positions of the oil-air meniscus: the bottom one with a zero contact angle on both solid surfaces, the top one with a larger contact angle on the defect on the right surface.

 

sion between phases $i$ and $j$, $s$ is the solid, $l$ is the liquid, $g$ is the gas phase, and $\gamma = \gamma_{lg}$. The strength of a wettability defect is proportional to the difference of spreading coefficients on the defect and on the clean substrate $\Delta S = S_d - S_0$. We define a nondimensional defect strength as

$$f = \frac{\Delta S d}{\gamma h} , \quad (1)$$

where $d$ is the defect diameter and $h$ the cell thickness. $f$ is the ratio of the surface energy required to cover the defect with liquid to the surface energy required to surround the defect with a liquid-gas interface. Weak defects ($f \ll 1$) are easily covered by the advancing liquid, while strong defects ($f \gg 1$) remain dry and trap gas bubbles.

When the cell is vertical, gravity should be taken into account and three length scales are involved in the problem: the cell thickness $h$, determining the hydrodynamic permeability $k = h^2/12$; the typical defect size $d$, determining the strength of the defects; and the capillary length $\lambda_c = \sqrt{\gamma/\rho g}$, determining the extent of the interface deformation. In the experiments reported here, the cell thickness is always much smaller than $\lambda_c$. As a result, the problem is quasi-two-dimensional and the description of the interface deformation on a single defect is analogous to a two-dimensional (2D) pendant drop or 2D meniscus problem. In addition, the defect size is generally also much larger than the cell thickness.

In Sec. II, we describe the experimental setup, the technique used to make the defects, and the image processing technique. In Sec. III, we report the experimental results for single defects, compare the observed contact line profiles with a two-dimensional theory and derive the force exerted by a defect on the contact line. In Sec. IV, we report preliminary results on the motion of the contact line over multiple defects.

## II. EXPERIMENTAL SETUP

The Hele-Shaw cell is made of two parallel float glass plates. The cell dimensions are 12 cm in the direction of motion and 7 cm in the transverse direction. Thin Mylar films are used as spacers between the glass plates. The cell gap $h$ can be varied from 25 to 100 $\mu$m. The parallelism of the glass plates and the variations of the gap width are checked by observing interference fringes under a sodium lamp illumination. For each experiment a new cell is built and the interference fringes pattern is recorded. The typical gap width variation throughout the cell is 5 $\mu$m. The precise gap width is measured with an interferometric technique before each experiment: the cell gap, acting as an interferometer, is placed in the optical path of a spectrophotometer. From the recorded transmission spectrum we derive the cell thickness.

The glass plates are reused and cleaned prior to each experiment with the following procedure. The first step is to put the plates in boiling water to remove glue. Most of the silicon oil is removed with cyclohexane. Then the glass plates are rinsed with acetone and then ethanol. The last step consists of putting the plates in a container with uv illumination and an oxygen flow to burn residual particles and solvents.

The wettability is controlled after the cleaning process by examining the spreading of a silicon oil droplet on one of the outer faces of the cell (all faces go through the same cleaning procedure). Wettability defects are made by spraying a concentrated alcohol soluble ink (Schwan-Stabilo HKS4) onto one of the glass plates. The spraying nozzle produces small droplets, ranging in size from 20 to 300 $\mu$m. The surface coverage is varied by changing the spraying time and the distance between the nozzle and the glass surface. The average size of the droplets can also be changed by altering slightly the geometry of the nozzle. A typical defect pattern is shown in Fig. 2. Single defects are made with a fine technical drawing pen.

When the solvent evaporates, the ink droplets leave a colored polymer layer on the glass surface. Contact angle measurements reveal that the dry ink is partially wetted by polydimethylsiloxane (PDMS): the measured contact angle is $\theta_d = 45°$, corresponding to a spreading coefficient $S_d = -6$ mN/m, while PDMS completely wets the clean glass surface ($S_0 \geq 0$). Isolated defects deposited on a small glass slide were observed with an atomic force microscope to determine the physical height and the roughness of the defect. The average defect thickness is around 5 $\mu$m, the outer part being slightly thicker, presumably a result of the drying process (Fig. 3). With the yellow ink that we use, the defect surface is smooth. Some other inks containing a dispersion of solid pigments produce defects with a rough surface and were rejected.

The advancing liquid is a silicone oil (polydimethylsiloxane, Rhône Poulenc 47 V20) with a viscosity $\eta = 20$ cP, a density of 0.95, and a surface tension $\gamma = 20.6$ mN/m. The capillary length derived from these physical properties is $\lambda_c = 1.45$ mm. The temperature of the flow cell is not controlled. The thermal expansion coefficient of the liquid is $1.07 \times 10^{-3}$/°C. The interface motion that would result from a 1 °C temperature variation is on

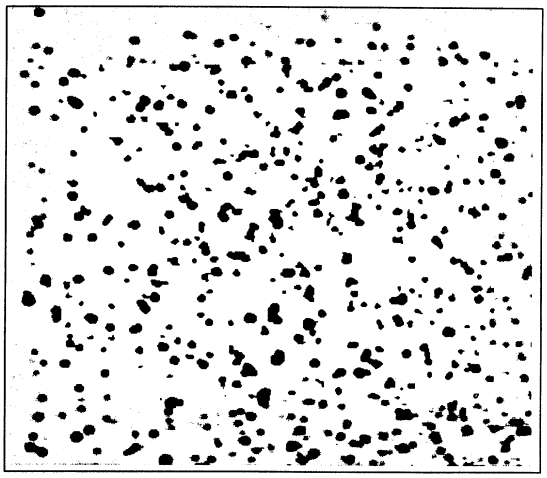

FIG. 2. Picture of a typical distribution of wettability defects made by the spraying technique. The actual picture size is $3.3 \times 3.1$ cm$^2$.

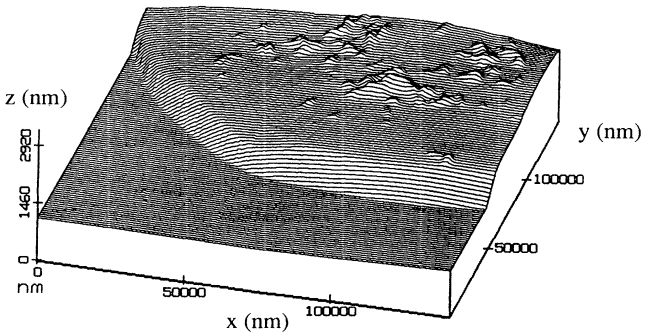


FIG. 3. Thickness profile of a defect, measured with an atomic force microscope.

the order of 10 $\mu$m, which is smaller than the meniscus thickness.

The liquid is injected in the cell, from the bottom edge, at a constant flow rate with a syringe pump. The range of available flow rates is $2.2\times10^{-5}-0.17$ cm$^3$/s, with corresponding contact line velocities $V=6$ $\mu$m/s–150 mm/s and corresponding capillary numbers $\mathrm{Ca}=\eta V/\gamma=6\times10^{-6}-0.15$. In all experiments reported here, the capillary number is within the range $(2-4)\times10^{-5}$.

The motion of the interface is recorded with a charge coupled device videocamera equipped with a $f/2.8$, 55-mm lens for microphotography. A color filter matching the ink hue is inserted in the light path to hide the defects and leave the interface as the only visible feature in the image. Digital pictures with 256 gray levels containing $512\times480$ pixels are obtained from the videosignal. The maximum sampling rate is limited by the rate of transfer to the computer main memory and is about 5 frames/s. The digitized pictures are transferred to a Silicon Graphics Iris Indigo workstation for processing. In the experiments reported here, the magnification is such that a pixel corresponds to 30–60 $\mu$m in the flow cell. In other words, the capillary length corresponds approximately to 30–70 pixels. Under diffuse illumination, the parts of the cell filled by the liquid appear slightly brighter. For very thin cells ($h=25$ $\mu$m), the meniscus itself is not visible, but for rather thick cells (around 100 $\mu$m), it appears as a black strip (because of the reflection of light rays on the interface). We generally use standard edge detection algorithms [13] to find the interface location: calculation of the image gradient with a Sobel operator (or a Sobel operator modified for noisy pictures), segmentation of the gradient image according to the gray level (edge or nonedge), and skeletonization of the edges. In some cases, we used another edge detection algorithm, derived from a minimum path search algorithm.

## III. QUASISTATIC DEFORMATION ON A SINGLE DEFECT AND PINNING TRANSITION

We have already reported observations of the interface motion past a single defect [8]. The main result is the existence of a pinning transition: weak defects produce a slight distortion of the interface which is released from the defect when the deformation becomes large enough. On the other hand, strong defects produce such a large distortion that the branches of the interface on either side of the defect coalesce to leave an air bubble trapped on the defect. This transition can be understood qualitatively by comparing the surface energy required to spread the liquid on the defect, $\Delta S d^2$, and the surface energy required to make a liquid-gas interface surrounding the defect, $\gamma h d$. The ratio of the two energies is the nondimensional defect strength $f$.

A more precise analysis involves the calculation of the energy $U$ of the distorted interface [14]. Let us recall the main results of this analysis, valid when the capillary number is small enough to assume that viscous stresses due to the liquid motion are negligible compared to the capillary pressure, i.e., when $\mathrm{Ca}\,(\lambda_c^2/h^2)\ll1$. When the cell is vertical, $U$ is the sum of interfacial and gravitational energy. Following de Gennes [12], we assume that the cross section of the meniscus connecting the two plates is a circle whose radius is determined by the contact angles. This is correct only when the thickness $h$ is small compared to the relevant horizontal length scale [15] and will not be true close to the defect where the contact angle should vary between $\theta_0$ and $\theta_d$, on a scale of order $h$. Neglecting this correction, the free energy is

$$U=T\int_0^L\sqrt{1+\zeta'^2}\,dx+\rho g h\int_0^L\int_0^{\zeta(x)}z\,dz\,dx\ , \tag{2}$$

where $\zeta(x)$ is the vertical coordinate of the contact line, $x$ is the horizontal coordinate, $L$ is the width of the flow cell and $T$ is an effective line tension. The line tension $T$ can be assumed to be the product of the surface tension and the length of interface in the $yz$ plane (normal to the cell)

$$T=\gamma h\frac{\pi-2\theta_0}{2\cos\theta_0}\ , \tag{3}$$

where $\theta_0$ is the contact angle outside the defect (Fig. 1). In what follows, $\theta_0$ will be assumed to vanish in the perfect wetting limit and we will ignore the existence of a precursor film. The effective line tension should then be $T=\gamma h(\pi/2)$.

The minimization of $U$ is a classical problem equivalent to the derivation of equilibrium shapes of two-dimensional pendant drops or two-dimensional meniscii [16,17]. The solution can also be obtained by equating the hydrostatic pressure $\rho g\zeta$ to the capillary pressure:

$$\Delta p_c=2\frac{\gamma}{h}-\frac{\pi}{4}\gamma C_{xz}\ , \tag{4}$$

where $C_{xz}$ is the curvature of the contact line [15]. Choosing the origin of the vertical axis such as $\zeta(+\infty)=0$, the contact line is then a curve with a curvature decreasing with the vertical coordinate. A general, convenient, parametric description of the interface is

$$\zeta=2\lambda_e\sin\left[\frac{\theta}{2}\right]\ , \tag{5}$$

where $\lambda_e$ is a modified capillary length and $\theta$ is the angle

between the horizontal and the tangent to the interface ($\tan\theta = d\zeta/dx$). When Eq. (3) for the line tension is used, the modified capillary length is $\lambda_e = \sqrt{\pi/2}\lambda_c$. On the other hand, the modified capillary length obtained from the Park-Homsy formula for the capillary pressure [Eq. (4)] is different: $\lambda_e = \lambda_{PH} = \sqrt{\pi/4}\lambda_c$. The difference between the two expressions for the line tension comes from the requirement of keeping a constant total curvature on the interface (for a constant capillary pressure). A small curvature of the contact line (in the $xz$ plane) requires a change in the shape of the meniscus in the $yz$ plane: the meniscus is no longer a circular arc. The calculation of this modified shape to the leading order in $\zeta_{xx}h$ gives the $\pi/4$ factor in the line tension, when the contact angle is zero [18].

When the amplitude of deformation is small enough compared to $\lambda_e$ ($\zeta' \approx \theta$), the contact line is described by an exponential function $\zeta = \zeta_{max}\exp(-x/\lambda_e)$. The lateral extent of the deformation is scaled by the effective capillary length, justifying the assumption used in the estimate of the free energy ($h \ll \lambda_e$). The modified capillary length also introduces a cutoff in the vertical extent of the solutions that cannot exceed $2\lambda_e$. In the pendant drop analogy, this is the maximum height of a drop that can be held by the interfacial tension.

Typical interface deformations are shown in Fig. 4, in the case of a rather weak defect ($f = 8$) unable to trap a bubble, and in Fig. 5, for a stronger defect ($f = 18$) trapping an air bubble. Both cases reveal some similar features: As the advancing fluid is pushed upward, the contact line is at first pinned on the bottom of the defect. The deformation of the line increases until the contact line starts advancing on the defect (lines marked $a$ in Figs. 4 and 5). The initial pinning on the defect edge is due to the sharp contrast of wettability and also to the small elevation change between defect and substrate.

On the weaker defect shown in Fig. 4, the maximum vertical deformation of the contact line is $0.6\lambda_c$. Once the line has moved approximately to the center of the defect, it is suddenly released and relaxes to its equilibrium straight configuration (line marked $r$ in Fig. 4).

On the stronger defect, the contact line pinches, an air bubble remains trapped on the surface, and the line relaxes (line marked $r$ in Fig. 5). To test the hypothesis made in the calculation of the contact line shape (namely, treating the problem as two dimensional), we plot in Fig. 5(b) the experimental contact lines as $\zeta/\lambda_e$ vs $\sin(\theta/2)$.

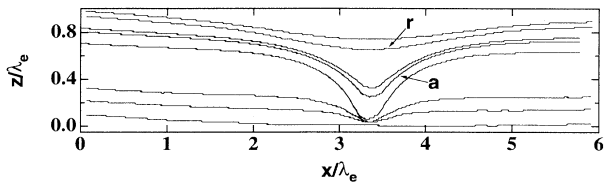


FIG. 4. Contact line deformations on a single defect of diameter $d = 0.56$ mm ($f = 8$) at different times. The coordinates are made dimensionless by the capillary length. The line labeled $a$ has begun to move over the defect. The line labeled $r$ has been released from the defect.

In this plot the interface should be a straight line with a slope 2. As can be seen in Fig. 5(b), the parts of the interface that are not pinned on the defect edge appear indeed to be close to straight lines with slopes independent of time. The effective capillary length determined from these plots on several defects is $\lambda_{expt} = 1.1 \pm 0.2$ mm. This is a much smaller value than the one calculated from the physical properties of the silicone oil and assuming a line tension given by (3): $\lambda_e = 1.86$ mm. However, the experimental value is consistent with the Park-Homsy capillary length $\lambda_{PH} = 1.30$ mm. Thus we are led to believe that the energy given in (3) describes the contact line correctly, with a line tension $T = \alpha\gamma h$, where $\alpha$ is a numerical factor found experimentally to be close to the value $\pi/4$ given by Park and Homsy.

Using the above result, we can now determine experimentally the energy involved in the contact line deformation. The total energy of the system is the sum of the gravitational energy of the liquid $E_g = \int \rho g z\, dV$ and of the interfacial energy $E_s = \int \gamma\, dS$. To get the energy involved in the deformation we have to subtract from the total energy the mean gravitational energy $E_{gm} = \frac{1}{2}\rho g h \langle\zeta\rangle^2$, where $\langle\zeta\rangle$ is the average vertical position of the contact line, and the mean surface energy $E_{sm} = TL$, where $L$ is the width of the flow cell. The mean gravity energy is supplied by the pump driving the liquid; the mean surface energy corresponds to a straight, horizontal contact line. In the two-dimensional approxi-

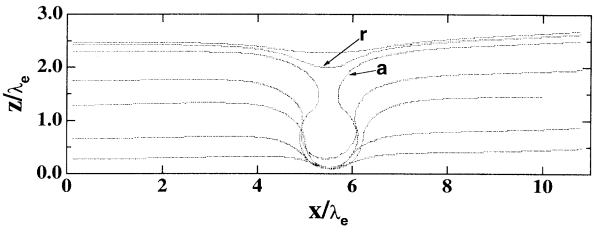


(a)

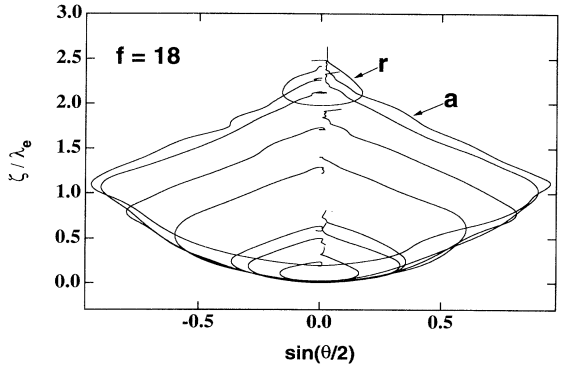


(b)

FIG. 5. Contact line deformations on a single defect of diameter $d = 2.25$ mm ($f = 18$) at different times: (a) lines shown in Cartesian coordinates made dimensionless by the capillary length, (b) lines shown in a parametric plot $\zeta/\lambda_e$ vs $\sin(\theta/2)$.

mation, $E_g = \rho g h \int z\, dz\, dx$ and $E_s = T \int ds$, where $s$ is the curvilinear coordinate along the interface in the $xz$ plane.

An additional term should be included in the energy; this term comes from the deformation of the interface in the $yz$ plane (normal to cell) due to the contact angle change between the substrate and the defect. Since the interface shape is described by Laplace's equation, the lateral extent of this deformation on each side of the defect is, at most, of order $h \ll d$. Consequently, the corresponding energy is approximately $\delta T l_d$, where $\delta T$ is the difference of line tension due to the contact angle change and $l_d$ is the length of contact line touching the defect. Assuming that $\delta T \sim T \Delta S/\gamma$ is small since $l_d$ is smaller than $d$, we will neglect this term in the following calculations.

The deformation energy calculated from the digitized interfaces for the cases shown in Fig. 4 and 5 is plotted as a function of the average contact line displacement in Figs. 6 and 7, respectively.

Figure 6 is an energy-displacement plot for a depinning event. At first, the deformation energy increases in proportion to the line displacement squared until the contact line starts to move over the defect. Then the energy drops sharply and levels until the contact line is freed from the defect. The sudden energy decrease occurring when the contact line moves past the leading edge of the defect is probably due to the physical height of the defect. This energy decrease varies substantially from one experiment to another and might be sensitive to the detailed shape and smoothness of the defect edge. The energy that we calculate does not include the deformation of the interface in the $y$ direction.

Figure 7 shows a bubble trapping event again, at first, deformation energy increases in proportion to the displacement squared until the contact line starts to move over the defect. There is correspondingly a leveling in energy until the contact line pinches off and the deformation energy relaxes to zero.

A parabola provides a reasonable fit to the energy-displacement data points (Figs. 6 and 7). The force exerted by the defect on the contact line is derived from the differentiation of this parabolic fit. Consequently, the defect force increases linearly with the displacement up to the depinning of the contact line. A similar result was found by Nadkarni and Garoff [9] in a different geometry. This linear force-displacement relation is expected for small deformations in the Hele-Shaw cell [14] and in a coating flow [19], but, so far, there is no theoretical prediction for large deformations.

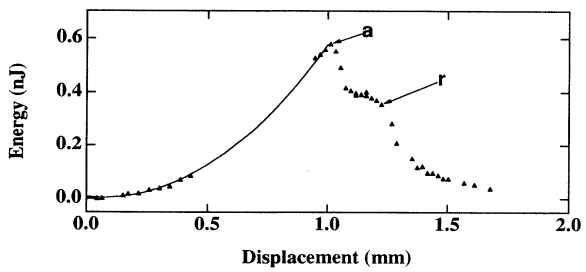


FIG. 6. Deformation energy vs displacement in the depinning event shown in Fig. 4. The line is a quadratic fit to experimental points up to point $a$.

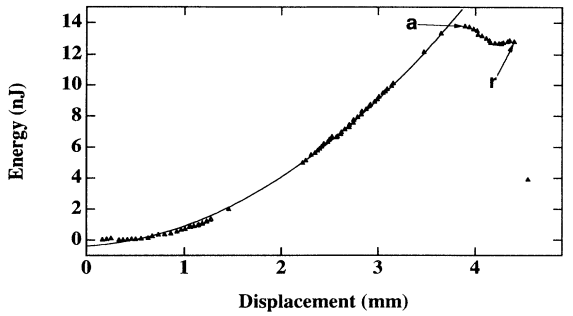


FIG. 7. Deformation energy vs displacement in the trapping event shown in Fig. 5.

From the fit to the energy-displacement curves, we determine the maximum force $F_m$ exerted on the contact line and plot $F_m^*$ ($F_m$ normalized by $d\Delta S$) as a function of the dimensionless defect strength $f$ (Fig. 8). For a bubble trapping event, we expect that the maximum force will be determined by the surface tension alone: The deformation increases until the force reaches the value $2Th$. In the pendant drop analogy, the drop grows until the interface is no longer able to sustain its weight. Then $F_m^*$ should be equal to $\pi/f$. For a depinning event, we expect the maximum force to increase in proportion to the defect size. Then $F_m^*$ should be constant. This is not the trend observed in Fig. 8, which shows rather that $F_m^*$ is constant for trapping events and that $F_m^*$ increases with $f$ when depinning occurs. The reason for this discrepancy might be the complex energy-displacement relation observed when the contact line moves over the defect edge. We find that the pinning transition occurs at $f = f_c \approx 7.5$. This critical value for the defect force is consistent with our previous experimental results [8].

A pinning transition similar to the one we observed is expected in the spreading of a liquid film of thickness $h$ on an horizontal solid substrate [19], a typical situation in spin coating. Again, the energy required to spread the liquid on the defect is $\Delta S d^2$ and the energy required to create the additional interfacial area to surround the de-

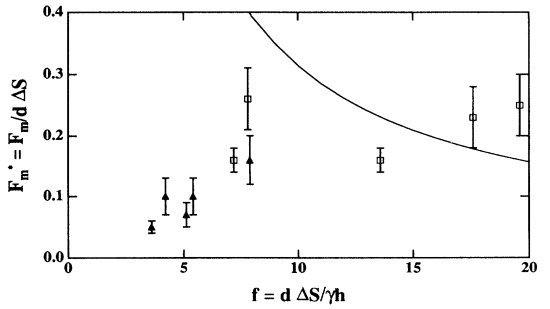


FIG. 8. Dimensionless maximum force exerted by a defect vs dimensionless defect strength. Open symbols, depinning events; filled symbols, trapping events; full line, $F_m^* = \pi/f$.

fect is of order $\gamma hd$. Sykes [20] calculated the axisymmetric equilibrium interface shapes around a circular defect and predicted the minimum thickness $h_c$ of a liquid film above to cover the defects. If we suppose that $\Delta S \ll \gamma$ (small wettability contrast) and if we neglect a logarithmic dependence on $\lambda_c/d$, Eq. (4) from Ref. [20] gives $h_c \approx fd$. This implies that the pinning transition should occur at a value of $f$ proportional to $h/d$ and not at a constant value. This remains to be tested by experiments. A more precise analysis of the pinning transition would require the calculation of the intermediate (non-axisymmetric) interface shapes, when the contact line is held on the leading edge of the defect.

## IV. MULTIPLE DEFECTS: QUASISTEADY INJECTION

We have recorded the motion of an interface moving at very small capillary number on a substrate contaminated by multiple defects. The experiments can be classified in two categories depending on the occurrence of dry spots behind the wetting front.

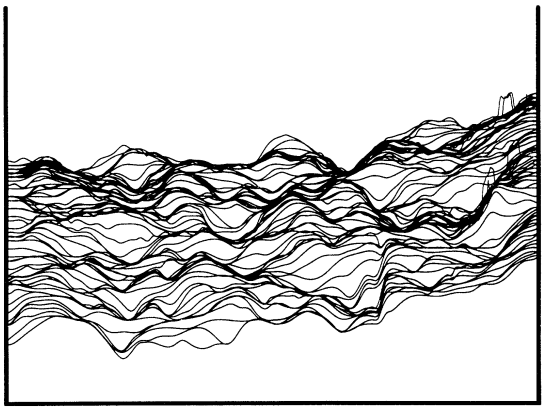

FIG. 10. Liquid advancing over multiple small defects. The positions of the wetting front equally spaced in time ($\Delta t = 10$ s) are determined by numerical image processing. Following image processing, the contact lines are approximated by smoothing spline fits. The vertical magnification is three times larger than the horizontal magnification.

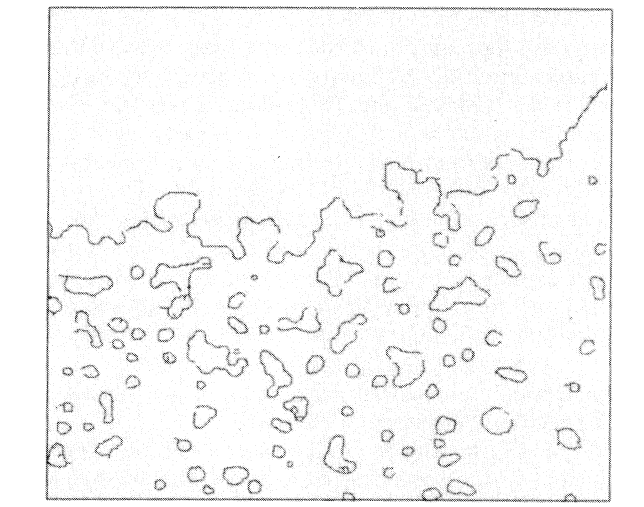

(a)

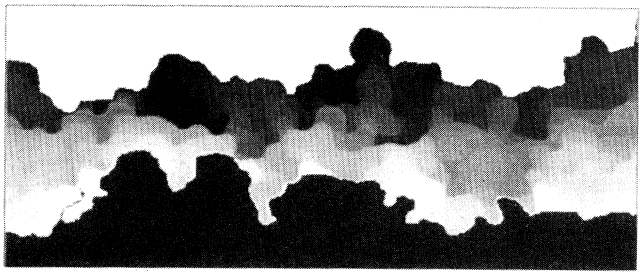

(b)

FIG. 9. Liquid advancing over multiple large defects. (a) Interface between oil and air determined by the image processing software. The upper line is the upward moving wetting front. Closed lines below the front are the edges of dry spots left behind the wetting line. (b) Positions of the wetting front equally spaced in time. Each gray level corresponds to a given time.

Nonwetted spots are obviously an undesirable result in a coating process. A photograph of the cell in such an "unfavorable" experiment is shown in Fig. 9(a). It is readily seen that the fluctuations of the wetting front are quite large: The maximum amplitude is of the order of the capillary length. In this example, the defects (shown in Fig. 2) produced by the spraying technique described in Sec. I are rather large and an appreciable number of them are larger than the critical size for bubble trapping. Behind the front, almost equally large spots remain dry. Figure 9(b) displays the positions of the wetting front at equally spaced time intervals for the same experiment. The contact line is temporarily trapped on the edge of large defects and moves forward by pinching and release of an air bubble.

On the other hand, when the average size of the defects is much smaller, there is only a weak distortion of the wetting front, no air bubble is trapped, and the substrate

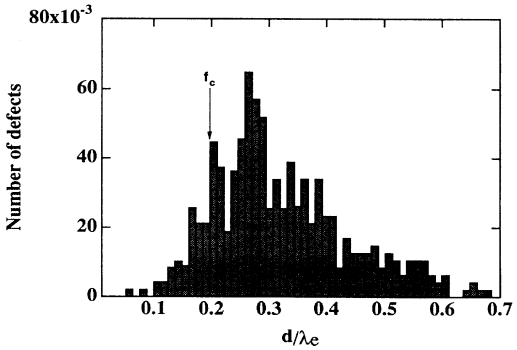


FIG. 11. Typical distribution of defect diameters (normalized by the capillary length). $f_c$ indicates the defect size corresponding to the critical pinning force.

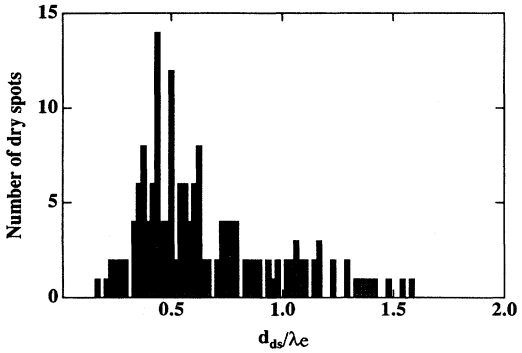


FIG. 12. Typical distribution of dry spot diameters (normalized by the capillary length).

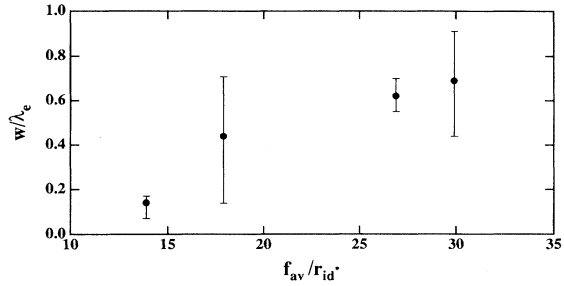


FIG. 13. rms fluctuation of the contact line position, normalized by the capillary length, as a function of the average defect force $f_{av}$ divided by $r_{id}$, the mean distance between defects.

is eventually completely wetted by the advancing liquid. Figure 10 displays the positions of the wetting front in such an experiment.

The quantitative observations we have done so far refer to the amplitude of fluctuation of the interface, the nonwetted surface fraction, and the size distribution of dry spots. The spraying technique used to make the defects does not allow a precise *a priori* control of the defect distribution. Consequently, we have not yet explored thoroughly the influence of mean defect size or defect density on the behavior of the interface.

Figure 11 shows a typical distribution of defect sizes, normalized by the modified capillary length $\lambda_e$ and the corresponding dimensionless defect strengths. This particular distribution was determined from a partial view of the cell shown in Fig. 9. Figure 12 shows the corresponding distribution of dry spots sizes in the same experiment. Most defects have a strength larger than the critical strength required to trap an air bubble. Therefore, a large number of dry spots are left behind the advancing liquid front. The size of the smallest dry spots corresponds to the size of the "critical defect." A few dry spots are twice as large as the largest defects, showing that a cluster of defects can act together on the contact line to trap a large air bubble.

We have repeated the experiment with other defect distributions. The main results from four experiments are reported in Table I; experiment I is the one shown in Fig. 9 and experiment IV is shown in Fig. 10. The defect distribution was analyzed from pictures similar to Fig. 2: In addition to the defect size already mentioned, we calculated $\sigma_{def}$, the surface fraction of the substrate covered by the defects, and, using a Voronoi tessellation, $r_{id}$, the mean distance between neighboring defects. We determined $\sigma_{dry}$, the surface fraction covered by dry spots at the end of the experiment, the size distribution of dry spots, and $w$, the amplitude of fluctuation of the wetting front as it moves through the cell. All length scales reported in Table I are normalized by the modified capillary length $\lambda_e$.

In experiments I–III the defects have a similar mean strength, larger than $f_c$, the critical strength for trapping; the nonwetted surface fraction increases with the defect surface fraction. In experiment IV the defects are much weaker, with a mean strength smaller than $f_c$ and, despite a defect surface fraction comparable to experiments I and II, no bubble trapping is observed. Since the defects are evenly distributed on the substrate, the wetting front does not experience a local force larger than $f_c$; the wetting of the substrate cannot be prevented by the defects. A coherent fluctuation of the spreading coefficient with an associated force larger than $f_c$ would be necessary to do so. The size of such a fluctuation is

TABLE I. Results from experiments with multiple defects. The following abbreviations are used: $\sigma_{def}$, surface fraction covered by defects; $\sigma_{dry}$, surface fraction covered by dry spots; $d_{min}$, $d_{av}$, and $d_{max}$, the minimum, average, and maximum diameters of the wettability defects, normalized by $\lambda_e$; $f_{min}$, $f_{av}$, and $f_{max}$, the corresponding minimum, average, and maximum defect strengths; $r_{id}$, the average distance between closest defects; $s_{min}$, $s_{av}$, and $s_{max}$, the minimum, average, and maximum diameters of the dry spots, normalized by $\lambda_e$; $w_{min}$, $w_{av}$, and $w_{max}$, the minimum, time average, and maximum of the rms contact line fluctuation, normalized by $\lambda_e$.

| Experiment | I | II | III | IV |
|---|---|---|---|---|
| $\sigma_{def}$ | 0.27 | 0.33 | 0.12 | 0.31 |
| $\sigma_{dry}$ | 0.18 | 0.35 | 0.08 | 0 |
| $d_{min}$, $d_{av}$, $d_{max}$ | 0.05, 0.31, 0.7 | 0.05, 0.24, 0.9 | 0.15, 0.29, 0.7 | 0.02, 0.12, 0.35 |
| $r_{id}$ | 0.8 | 0.8 | 0.6 | 0.25 |
| $f_{min}$, $f_{av}$, $f_{max}$ | 2.6, 16, 36 | 2.6, 12.5, 47 | 7.8, 15, 36 | 0.5, 3, 8.7 |
| $s_{min}$, $s_{av}$, $s_{max}$ | 0.2, 0.7, 1.5 | 0.22, 0.43, 1.5 | 0.2, 0.33, 0.5 | |
| $w_{min}$, $w_{av}$, $w_{max}$ | 0.55, 0.62, 0.70 | 0.44, 0.69, 0.91 | 0.14, 0.44, 0.71 | 0.073, 0.14, 0.17 |

equivalent to the anchoring length defined by de Gennes [12].

The amplitude of fluctuation of the wetting front $w$, calculated as the root mean square fluctuation of $\zeta(x)$, fluctuates with time during a given experiment, but there is no long term drift of $w$. This is not surprising when bubble trapping occurs: In this regime, the largest fluctuation is determined by the capillary length which determines also the maximum size for a stable bubble. Similarly, the amplitude of fluctuation is also time independent, over long time scales, when there is no trapping (experiment IV).

From the results in Table I, we try to correlate the amplitude of fluctuation with the defect distribution. The vertical extent of the front should be determined by, on the one hand, a balance between the hydrostatic pressure $\rho g w$ acting over an area $h r_{\mathrm{id}}$, where $r_{\mathrm{id}}$ is the mean distance between defects, and, on the other hand, the defect force $f = d\Delta S$. This leads to

$$w^* = \frac{f}{r_{\mathrm{id}}^*} , \tag{6}$$

where $w^*$ and $r_{\mathrm{id}}^*$ are, respectively, the fluctuation amplitude and the distance between defects, both normalized by the capillary length. Figure 13 displays the normalized amplitude fluctuations as a function of the average defect force $f_{\mathrm{av}}$, divided by $r_{\mathrm{id}}$, the mean distance between defects.

## V. CONCLUSION

We have analyzed the deformation of contact lines on isolated wettability defects. The contact line shapes can be derived from a two-dimensional approximation of the flow. An effective tension for the contact line is determined from the experiments; it is consistent with the analysis done by Park and Homsy. Our main findings are the existence of a critical defect strength to pin the interface and the linear force-deformation relationship. The forces involved in the interface deformation are very small (on the order of 1 $\mu$N) and could not be measured directly. They were inferred from the shape of the contact line, using a hypothesis considering only the deformation in the plane of the flow cell. These results were obtained in the peculiar geometry of the imperfect Hele-Shaw cell and they should be applicable directly in similar flows, such as the injection of an adhesive between two solid surfaces. They can probably be generalized to other coating flows, replacing the thickness of the Hele-Shaw cell by the thickness of the liquid layer advancing on the solid in the definition of the dimensionless defect strength. However, the problem of coating flows is probably more complex because of the intrinsic instability of the capillary ridge at the leading edge of the liquid layer. Defects should play a crucial role in the triggering of the instability.

The vertical position of the flow cell, required to observe flat interfaces in the single-defect experiments, introduces the capillary length scale which provides an upper bound for the interface deformation. The geometric properties of the wetting fronts moving over many defects are influenced to a large extent by the capillary length. A similar study, with the cell in the horizontal position to get rid of gravity effects, is obviously desirable.

Our future work includes the study of the evolution of the interface roughness (amplitude and scaling properties) as a function of the density of defects. A precise control of the defect distribution is now possible through an optical lithography technique.

## ACKNOWLEDGMENTS

This work is supported by Institut Français du Pétrole and Centre National d'Etudes Spatiales. We thank E. J. Hinch for indications about the nonlinear shape of the interface and S. Roux for help in data analysis and stimulating discussions. The core of the image processing software was written by Ralph Goodwin. The interferometric cell thickness measurements were performed at Laboratoire d'Optique Physique, ESPCI.

[1] P. G. de Gennes, Rev. Mod. Phys. **57**, 827 (1985).
[2] C. P. Wong (private communication).
[3] P. Concus, R. Finn, and M. Weislogel, Science Review for United States Microgravity Laboratory Space Shuttle Flight, Lawrence Berkeley Laboratory Report No. 34819, 1993 (unpublished).
[4] J. Drelich and J. D. Miller, Colloids Surf. **69**, 35 (1992).
[5] F. H. Chang, *Engineered Materials Handbook, Vol. 3 Adhesive and Sealants* (ASM International, 1990).
[6] S. Lazare, V. Granier, P. Lutgen, and G. Feyder, Rev. Phys. Appl. **23**, 1065 (1988).
[7] J. M. Di Meglio and D. Quéré, Europhys. Lett. **11**, 163 (1990).
[8] J. F. Duprat, M. Fermigier, F. Goulaouic, and P. Jenffer, C. R. Acad. Sci. **314**, 879 (1992).
[9] G. D. Nadkarni and S. Garoff, Europhys. Lett. **20**, 523 (1992).
[10] J. A. Marsh and A. M. Cazabat, Europhys. Lett. **23**, 45 (1993).
[11] J. M. Di Meglio, Europhys. Lett. **17**, 607 (1992).
[12] P. G. de Gennes, J. Phys. **47**, 1541 (1986).
[13] A. K. Jain, *Fundamentals of Digital Image Processing* (Prentice-Hall, Englewood Cliffs, NJ, 1989).
[14] L. Limat, C. R. Acad. Sci. **314**, 1011 (1992).
[15] C.-W. Park and G. M. Homsy, J. Fluid Mech. **139**, 291 (1984).
[16] E. Pitts, J. Fluid Mech. **59**, 753 (1973).
[17] A. D. Myshkis, V. G. Babskii, N. D. Kopachevskii, L. A. Slobozhanin, and A. D. Tyuptsov, *Low-Gravity Fluid Mechanics* (Springer, New York, 1987).
[18] E. J. Hinch (private communication).
[19] J. F. Joanny and P. G. de Gennes, J. Chem. Phys. **81**, 552 (1984).
[20] C. Sykes, C. R. Acad. Sci. **313**, 607 (1991).

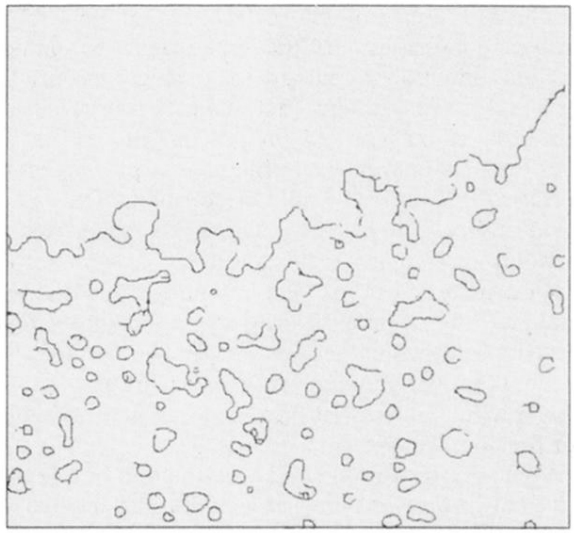

(a)

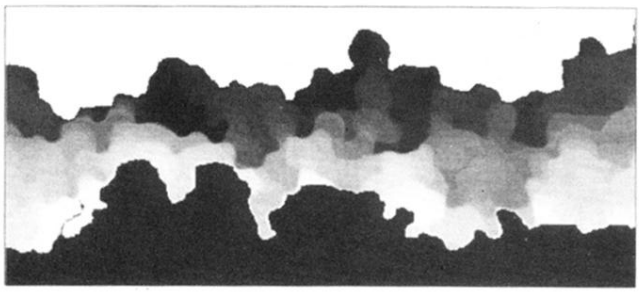

(b)

FIG. 9. Liquid advancing over multiple large defects. (a) Interface between oil and air determined by the image processing software. The upper line is the upward moving wetting front. Closed lines below the front are the edges of dry spots left behind the wetting line. (b) Positions of the wetting front equally spaced in time. Each gray level corresponds to a given time.